RESEARCH ARTICLE

ADVANCED FUNCTIONAL MATERIALS
www.afm-journal.de

Interplay of Structure, Charge-Carrier Localization and Dynamics in Copper-Silver-Bismuth-Halide Semiconductors

Leonardo R. V. Buizza, Harry C. Sansom, Adam D. Wright, Aleksander M. Ulatowski, Michael B. Johnston, Henry J. Snaith, and Laura M. Herz**

Silver-bismuth based semiconductors represent a promising new class of materials for optoelectronic applications because of their high stability, all-inorganic composition, and advantageous optoelectronic properties. In this study, charge-carrier dynamics and transport properties are investigated across five compositions along the $AgBiI_4$–CuI solid solution line (stoichiometry $Cu_{4x}(AgBi)_{1-x}I_4$). The presence of a close-packed iodide sublattice is found to provide a good backbone for general semiconducting properties across all of these materials, whose optoelectronic properties are found to improve markedly with increasing copper content, which enhances photoluminescence intensity and charge-carrier transport. Photoluminescence and photoexcitation-energy-dependent terahertz photoconductivity measurements reveal that this enhanced charge-carrier transport derives from reduced cation disorder and improved electronic connectivity owing to the presence of Cu^+. Further, increased Cu^+ content enhances the band curvature around the valence band maximum, resulting in lower charge-carrier effective masses, reduced exciton binding energies, and higher mobilities. Finally, ultrafast charge-carrier localization is observed upon pulsed photoexcitation across all compositions investigated, lowering the charge-carrier mobility and leading to Langevin-like bimolecular recombination. This process is concluded to be intrinsically linked to the presence of silver and bismuth, and strategies to tailor or mitigate the effect are proposed and discussed.

1. Introduction

The last decade has seen a remarkable rise of interest in metal-halide perovskite materials, notably owing to their successful application in photovoltaics[1,2] and light-emitting diodes.[3,4] Although lead-halide perovskites have been the cornerstone of this success, achieving power conversion efficiencies (PCEs) of over 25% in solar cell devices,[5] attention has shifted toward alternative lead-free all-inorganic materials,[6–8] because of concerns around both the intrinsic stability[9–12] and potential toxicity[8,13] of lead-based perovskites. For conventional metal-halide perovskites, which have a stoichiometry of ABX_3, attempts have been made to replace the lead cation (Pb^{2+}) with homovalent Sn^{2+} in photovoltaic devices.[14,15] However, these materials have struggled to achieve PCEs comparable to their lead-based counterparts owing to the easy formation of tin vacancies, which greatly inhibit device performance.[16–18] Alternatively, the heterovalent substitution of Pb^{2+} with mono- and trivalent cations has led to the exploration of a variety of so-called “double perovskites”,[19,20] which have a general formula $A_2BB'X_6$ and the same corner-sharing octahedral network as conventional lead-halide perovskites,[21] with the most commonly investigated material being $Cs_2AgBiBr_6$.[6,22,23] Although solar cells with PCEs above 3% have been demonstrated with $Cs_2AgBiBr_6$,[24] its indirect band gap necessitates large film thicknesses for functional devices, in turn requiring large charge-carrier diffusion lengths, which has prevented rapid improvements in device performance.[23–26] Recent work has thus expanded to other silver-bismuth semiconductors that share certain structural and electronic properties with metal-halide perovskites, such as silver-bismuth-iodides,[27,28] $Rb_4AgBiBr_9$,[7] layered $(BA)_2CsAgBiBr_7$ (BA = butylammonium),[29] and $(AE2T)_2AgBiI_8$ (AE2T = 5,5'-diylbis(aminoethyl)-[2,2'-bithiophene]),[30] Cu_2AgBiI_6,[31] as well as a variety of bismuth-containing materials.[32–37]

A crucial step in the development of high-performance semiconductors is the realization of a complete understanding of the charge-lattice interactions which influence critical optoelectronic parameters such as charge-carrier mobilities

---

L. R. V. Buizza, H. C. Sansom, A. D. Wright, A. M. Ulatowski,
M. B. Johnston, H. J. Snaith, L. M. Herz
Department of Physics
University of Oxford
Clarendon Laboratory, Parks Road, Oxford OX1 3PU, UK
E-mail: henry.snaith@physics.ox.ac.uk; laura.herz@physics.ox.ac.uk

L. M. Herz
TUM Institute for Advanced Study
Technische Universität München
Lichtenbergstraße 2a, 85748 Garching bei München, Germany

The ORCID identification number(s) for the author(s) of this article can be found under https://doi.org/10.1002/adfm.202108392.

DOI: 10.1002/adfm.202108392

and energetic relaxation. For ionic materials with weak-to-intermediate charge-lattice couplings, such as $MAPbI_3$, GaAs or layered Ruddlesden–Popper perovskites, the formation of large polarons leads to a slight increase in charge-carrier effective mass[38,39] but does not otherwise substantially alter charge-carrier energetics and dynamics.[21,40] Thus the formation of large polarons[41,42] in lead-halide perovskite semiconductors[21,43,44] has been underpinning their successful implementation in light-emitting and photovoltaic devices that can rival commercial systems. However, some of the more recently developed lead-free metal halide semiconductors, such as silver-bismuth based materials,[23,26,45–47] have been shown to exhibit much stronger charge-lattice couplings leading to the formation of states that have been described as a "small polaron," as a self-trapped charge, or as the formation of a color center.[48–50] In this case of stronger couplings, more substantial impacts on photoluminescence energies and charge-carrier dynamics and mobilities can be observed,[21,50] making a careful analysis of such effects central to an assessment of their suitability in various device applications.

In this context, it must be suspected that the presence of strong charge-carrier localization effects may be a key reason behind the underperformance of silver-bismuth semiconductors to date: recent studies have shown the formation of small polarons localized within a few picoseconds in both $Cs_2AgBiBr_6$[23,26,45–47] and Cu_2AgBiI_6.[51] In their study of $Cs_2AgBiBr_6$, Wu et al.[45] draw attention to two key factors contributing to strong self-trapping in this material: the structural instability and strong acoustic-phonon deformation potentials present in bismuth[52,53] and Bi-based compounds such as Bi_2Te_3[33,34] or BiI_3,[35] and the soft nature of silver-halide bonds that are easily distorted, which together lead to charge-carrier localization.[54] At a fundamental level, such ease of structural distortion can be interpreted in terms of the greater ionicity (i.e., a greater difference in electronegativities) of silver-halide and bismuth-halide bonds in such materials, relative to lead-halide bonds, which imparts larger electron–phonon couplings in silver-bismuth semiconductors.[23,26,37,46,51] In our previous work on $Cs_2AgBiBr_6$[23] and Cu_2AgBiI_6[51] we have further linked the localization of charge carriers to the low electronic dimensionality of such silver-bismuth materials,[55,56] which leads to individual structural units (such as octahedra) to be electronically isolated from each other, acting as a barrier to efficient charge-carrier transport. Taken together, these works point toward two potential causes for charge-carrier localization in silver-bismuth materials: first, the easy structural distortion of bismuth-based systems and "soft" silver-halide bonds; second, the low electronic dimensionality that prevails in materials with alternating silver and bismuth structural units. Although similar charge-carrier localization effects have been observed across these and other materials,[7,30,32,36,37,57] an holistic understanding of the interplay between crystal structure, electronic structure, and optoelectronic properties in silver-bismuth materials, and how such effects may be tuned through stoichiometric engineering, has remained lacking thus far.

Here, we investigate five materials along the $AgBiI_4$–CuI solid solution line ($Cu_{4x}(AgBi)_{1-x}I_4$ with x = 0, 0.09, 0.2, 0.33, 0.6) to reveal how changes in crystal structure and composition influence charge-carrier dynamics, localization, and transport. A combination of X-ray diffraction (XRD), photoluminescence (PL) and optical absorption measurements demonstrate that these silver-bismuth semiconductors display a promising mix of the optoelectronic properties found in $MAPbI_3$, notably of strong optical absorption, low exciton binding energies, bandgaps in the visible range and charge-carrier mobilities well above $1\,cm^2\,V^{-1}\,s^{-1}$. Further, ultrafast optical-pump terahertz-probe (OPTP) spectroscopy with a variable pump fluence and photon energy allows us to probe small polaron motion and reveals how charge-carrier relaxation, localization, and recombination interact following photoexcitation. We find that the addition of Cu^+ improves the photoluminescence intensity and charge-carrier mobility substantially, although this is accompanied by a slight decrease in optical absorption strength and a faster charge-carrier localization rate. Further, we find that reduced exciton binding energies and increased charge-carrier mobilities with rising Cu^+ content can be well-explained by a reduction in charge-carrier effective mass, which we attribute to increased contributions from copper states at the valence band minimum that lead to increased band curvature. Interestingly, our measurements reveal that bimolecular (radiative) recombination is not well-described by a band-to-band radiative-balance model, as it exhibits inverse trends in optical absorption strength and bimolecular recombination rate constants. Instead the small-polaron recombination rate constants appear to increase with rising charge-carrier mobilities, similar to the Langevin-type recombination found in organic semiconductors. Finally, we use the results presented here to draw wider conclusions around charge-lattice interactions in silver-bismuth semiconductors, including how these effects can be tailored or mitigated according to the potential target application of such materials.

2. Structural Discontinuity and Enhanced Electronic Connectivity with Increasing Copper Content

Replacement of equimolar amounts of Ag^+ and Bi^{3+} with Cu^+ will lead to changes in the composition of the materials investigated here, which we investigate using scanning electron microscopy (SEM) imaging and energy-dispersive X-ray (SEM-EDX) analysis. Thin films of $Cu_{4x}(AgBi)_{1-x}I_4$ with nominal (aimed-for) compositions of $x = 0$ ($AgBiI_4$), 0.09 ($Cu_{0.4}AgBiI_{4.4}$), 0.2 ($CuAgBiI_5$), 0.33 (Cu_2AgBiI_6), and 0.6 (Cu_6AgBiI_{10}) were deposited onto glass microscopy slides and z-cut quartz substrates. The $x = 1$ composition (CuI) was not investigated as it has a very high band gap (3.0 eV[58–60]) and a zincblende structure with tetrahedral sites,[61] rendering it incomparable to the silver- and bismuth-containing materials which have a ≈2 eV band gap and edge-sharing octahedrally-coordinated structure (discussed below and in refs. [27,31]). See the Supporting Information for details of the sample fabrication and experimental techniques used.

The exact compositions measured via SEM-EDX for these films show good agreement with the nominal (expected) compositions across the whole range (see **Figure 1**a and Figure S1, Supporting Information), albeit with a slight iodine deficiency present. The SEM images (Figure S2, Supporting Information) also show less uniform surface coverage with increasing x, indicating a rise in surface roughness—a trend which we discuss below in relation to the measured PL intensity and bimolecular

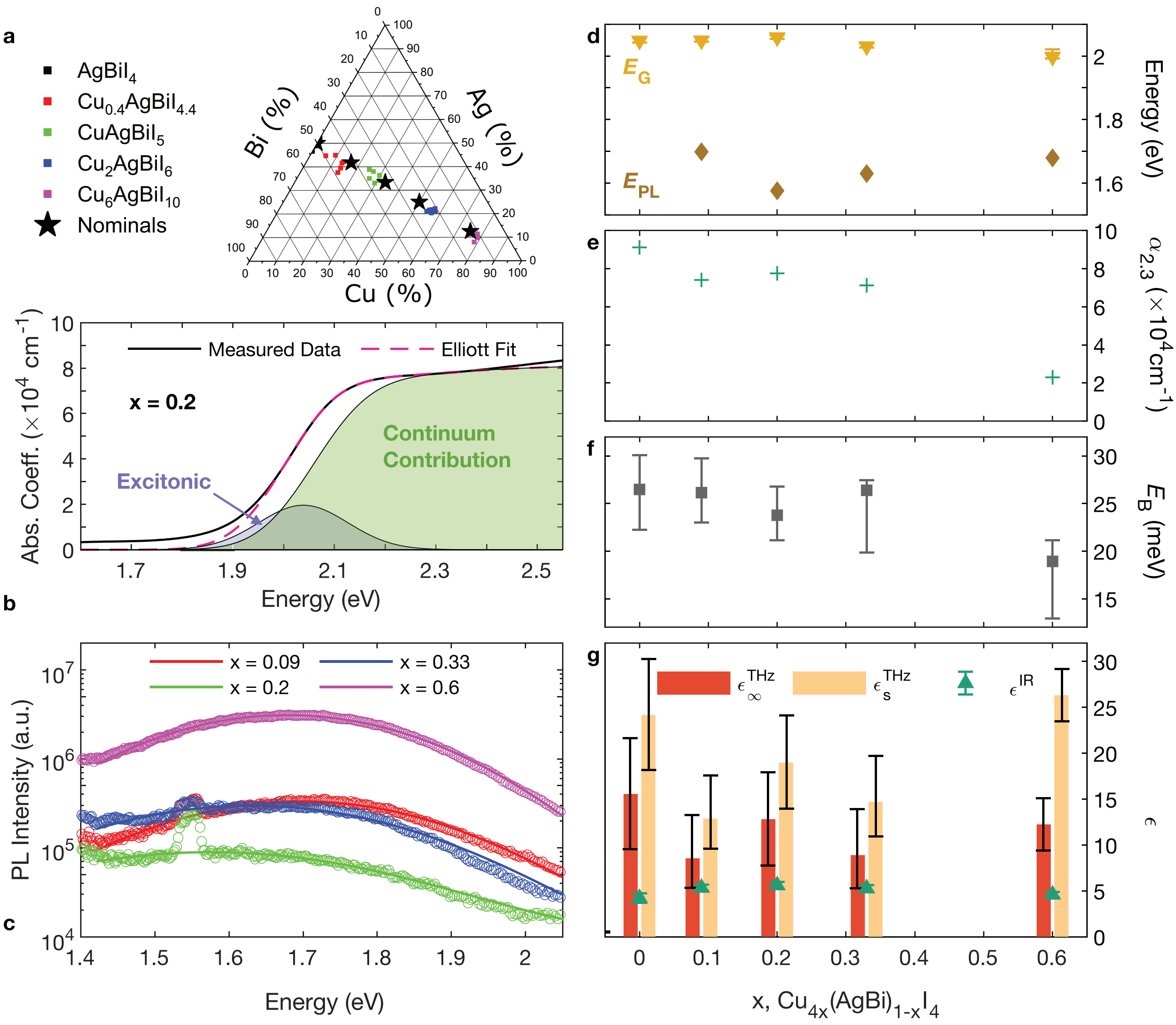

Figure 1. a) Nominal (black stars) and measured (colored squares) chemical compositions, measured using SEM EDX, of the five Cu$_{4x}$(AgBi)$_{1-x}$I$_4$ compositions investigated in this work. b) UV–visible absorption spectrum of CuAgBiI$_5$ ($x = 0.2$) (black line), and fit according to Elliott's theory[66] (pink dashed line). The excitonic and Coulomb-enhanced free-carrier contributions to the absorption are shown are the shaded blue and green areas, respectively. (See Supporting Information for equivalent plots for the other four compositions, and for details of the fitting.) c) Steady-state photoluminescence from thin films of four compositions (shown as open circles), following photoexcitation at 398 nm at an intensity of 265 Wcm^{-2}. The spectra are fitted with Gaussian lineshapes, with the fits shown as solid lines. (The peak around 1.55 eV present in some of the spectra is caused by the second-order diffraction peak of the 3.1 eV excitation light.) d) Value of the band gap energy E_G (yellow triangles) extracted from the Elliott fits and peak PL energy E_{PL} (brown diamonds) extracted from the Gaussian fits, for each composition. e) Value of the optical absorption coefficient at 2.3 eV, used as an indication of the overall optical absorption strength for each composition. f) Value of the exciton binding energy E_B extracted from the Elliott fits, for each composition. Error bars were obtained by varying the range of energies to which the fits were applied. g) Measured values of the dielectric function ε. Values of the THz high-frequency (red bars) and static (cream bars) values of the dielectric function $\varepsilon_{\infty/s}^{THz}$ were extracted from THz absorption measurements. Values of the dielectric function in the infra-red ε^{IR}, were calculated from reflection and transmission spectra between 1200–1300 nm (see Supporting Information for details of calculations).

recombination rate constants for the thin films studied here. Further, in order to understand how the addition of copper influences the crystal structure across the solid solution line, X-ray diffraction measurements were carried out for spin-coated thin films deposited on both glass microscopy slides and on z-cut quartz (see Figures S3 and S5, Supporting Information). These show excellent agreement between the two substrate types, and indicate a small amount of BiOI impurity present in the thin films deposited on the microscopy slides, which is however absent in the thin films on quartz, as discussed in more detail in the Supporting Information. We also take this as an indication that the small iodine deficiency present in the thin films on microscopy slides is less substantial for the thin films deposited on quartz. We use the thin films deposited on z-cut quartz for all of the optoelectronic measurements and analysis presented in the main text.

Previous studies of $AgBiI_4$, $CuAgBiI_5$, and Cu_2AgBiI_6 (x = 0, 0.2, 0.33) have found the crystal structure of these materials to have high levels of atomic disorder, notably with low Cu^+ occupancy on tetrahedral sites, and to contain octahedral networks of varying dimensionality that form depending on the amount of Ag^+ and Bi^{3+}.[27,31,62] Fitting of the a and c lattice parameters for the five compositions studied here, derived from the XRD measurements, show an interesting discontinuity moving from $x \leqslant 0.2$ to $x \geqslant 0.33$, which is also reflected in the calculated unit cell volumes (see Figure S4, Supporting Information). We argue that this discontinuity corresponds to a change in the crystal structure where the octahedral network transitions from 3D in $CuAgBiI_5$ to 2D in Cu_2AgBiI_6 following substitution of octahedral site occupancy (Ag^+ and Bi^{3+}) with tetrahedrally-coordinated Cu^+.[27,31,62]

We also suggest that the addition of Cu^+ leads to a general increase in electronic connectivity, although the significant disorder present in these materials complicate the verification of this via density-functional-theory (DFT) approaches.[27,31] Crystallographic and DFT-based studies of $AgBiI_4$[27] and $CuBiI_4$[63,64] have shown that the conduction band minimum of these materials consists of bismuth and iodine electronic p-states, and the valence band maximum comprises mainly iodine p-states, with some contributions from silver or copper electronic states, respectively. Notably, this result holds across all of the multiple potential crystal structures that these materials can take as the lowest-energy configuration.[27,64] Although the exact crystal structure of the Cu-Ag-Bi-I materials investigated here will also vary (namely, 2D vs. 3D octahedral networks), we suggest that an increase in proportion of tetrahedrally-coordinated Cu^+ should lead to two effects: changes in the electronic structure of the VBM, and increased electronic connectivity. The former arises from copper mainly contributing to electronic states in the valence band, as has been shown for Cu_2AgBiI_6.[31] The latter point follows from the increased availability of tetrahedrally-coordinated sites facilitated by the cubic close-packed iodide sublattice, relative to octahedrally-coordinated sites. This point is of great importance to silver-bismuth based materials, given that neighboring silver- and bismuth-based octahedra have been shown to be electronically isolated[55,56,65] owing to the lack of spatial overlap of contributions from the silver and bismuth electronic states. Thus, as the octahedral network changes with reduced Ag-Bi content, the increased presence of tetrahedral copper leads to increased spatial and electronic overlap between different crystallographic sub-structures, improving the electronic connectivity across the material.

Overall, an increase of x in the thin films of $Cu_{4x}(AgBi)_{1-x}I_4$ is expected to yield two significant changes in the composition and crystal structure: a change in the octahedral network from 3D to 2D with decreasing presence of octahedral Ag^+ and Bi^{3+}, and an increased tetrahedral occupancy and increase in tetrahedral connectivity of Cu^+, with the iodide sublattice remaining largely unchanged. Both changes influence the electronic band structure of the materials as well as the strength of interactions between charge carriers and the lattice. We now discuss the influence of Cu^+ content and structural changes on the optoelectronic properties and formation of small polarons across the silver-bismuth materials investigated here, based on results from a variety of spectroscopic measurements.

3. Influence of Copper on the Electronic Structure

In order to probe the viability of these proposed concepts, and to understand how the addition of copper alters the electronic band structure in these silver-bismuth materials, we carried out UV–visible absorption measurements on spin-coated thin films, deposited on z-cut quartz substrates. To extract values for band gap energies and exciton binding energies, we applied fits to the absorption spectra near their onsets according to Elliott's theory,[66] which describes the electronic transitions between parabolic bands of a semiconductor in the presence of Coulomb interactions. We find that the band gap energy decreases slightly from 2.05 eV for x = 0 ($AgBiI_4$) down to 2.00 eV for x = 0.6 (Cu_6AgBiI_{10}), accompanied by a corresponding reduction in the exciton binding energy from 27 to 19 meV. (See Figure 1b for the steady-state optical absorption of $CuAgBiI_5$ (x = 0.2, black line), as well as a fit to the spectrum according to Elliott's theory (pink dashed line), and see Figure S6a–d, Supporting Information for fits to the remaining compositions). Further, we use the magnitude of the absorption coefficient at 2.3 eV, $\alpha_{2.3}$, as a proxy for the overall above-band gap absorption strength; this takes a high value for $AgBiI_4$ (x = 0), above 8×10^4 cm^{-1}, but falls with increasing x, markedly so in the case of Cu_6AgBiI_{10} (x = 0.6). As the relative proportion of Bi^{3+} and Ag^+ is diluted upon increasing x content (addition of Cu^+), the strength of the above-band gap absorption decreases correspondingly, which we attribute to much stronger contributions to the above-gap electronic transitions from silver and bismuth, relative to copper. Indeed, previous studies have shown that at an energy of 2.3 eV, BiI_3 (9.7–16.5 × 10^4 cm^{-1})[67] and AgI (6.9–11.2 × 10^4 cm^{-1})[68,69] have a much larger absorption coefficient than CuI (0.5–0.9 × 10^4 cm^{-1}),[60] in excellent agreement with the trend observed here.

The exciton binding energies extracted from the Elliott fits are comparable to thermal energies at room temperature (≈26 meV), and somewhat higher than that in $MAPbI_3$ of 12 ± 7 meV,[43] indicating that excitons likely do not play a substantial role in the charge-carrier dynamics in the silver-bismuth materials studied here. Further, the measured values are much lower than the several hundred meV reported for Cs_2AgBiX_6 (X = Br, Cl),[23,37,70] which is likely associated with the somewhat lower direct band gaps in the materials investigated here,[71] as well as differences in charge-carrier effective masses, discussed in more detail below.

The exciton binding energy depends generally on the dielectric screening and electron-hole reduced mass M as $E_B \propto \frac{M}{\varepsilon_r^2}$. An insight into the origin of such suitably low exciton binding energies must therefore center on these two parameters. We begin by investigating the dielectric screening in these silver-bismuth materials, determining values of the dielectric function ε from fits to the reflectance and transmittance between 1200–1300 nm (ε^{IR}), and also from THz absorption spectroscopy (which yields ε_∞^{THz} and ε_s^{THz}). For all of the silver-bismuth materials studied here, E_B lies at energies in between the range probed using the THz absorption measurements (2–11 meV) and the infra-red limit of the optical absorption measurements carried out (≈0.95 eV). The appropriate value for estimating E_B is thus somewhere between the values of ε^{IR} obtained in the infra-red and the high-frequency constant in the THz range

$\varepsilon_{\infty}^{\text{THz}}$,[43] and we plot the measured values in Figure 1g. (See Supporting Information for a detailed discussion of the calculation methods for these values of the dielectric function).

Overall, we find the dielectric screening across the compositional range studied here to be similar to that encountered in MAPbI_3: all values lie close to or above the value for MAPbI_3 at frequencies corresponding to its exciton binding energy ($\varepsilon_{\infty}^{\text{THz}} \approx 5.4$).[43] This finding implies that the higher exciton binding energies found here, roughly twice the value encountered in MAPbI_3, are caused by enhanced charge-carrier effective masses, rather than reduced dielectric screening,[43,72] a result which is in good agreement with the lower charge-carrier mobilities obtained here (given that $\mu \propto \frac{1}{m^*}$, as discussed below). Further, there is no trend in dielectric screening with composition, but the reduction in exciton binding energy with x (from 27 to 19 meV) correlates very well with the increased charge-carrier mobilities (reduced effective mass) with x discussed below, suggesting that the significant consequence of the addition of copper is the alteration of the curvature of the electronic bands around the VBM.

Overall, the optical absorption spectra and dielectric values of the silver-bismuth materials investigated here seem to combine the best of MAPbI_3 and $\text{Cs}_2\text{AgBiBr}_6$, in that they have direct band gaps in the optical range with strong absorption above the absorption onset, exciton binding energies similar to thermal energies and middling dielectric screening, whilst remaining fully inorganic and lead free. Further, the substitution of Ag^+ and Bi^{3+} with Cu^+ is found not to alter the band gap energy of these materials substantially, but to cause a reduction in exciton binding energy, which we attribute to decreased charge-carrier effective masses resulting from an increased curvature around the band extrema.

4. Charge-Carrier Localization and Energetics are Intrinsically Linked to the Presence of Ag and Bi

Charge-carrier localization may lead to changes in the energetic distribution of states present in a semiconductor.[21,73] In order to understand such changes, we carried out measurements of the steady-state photoluminescence, which reveal highly Stokes-shifted PL spectra with large full-width half-maxima (FWHM, see Figure 1c and Figure S10, Supporting Information). The spectra were measured for thin films following photoexcitation at 398 nm at an excitation intensity of 265 W cm^{-2} (the PL was too faint to be distinguished from background noise for AgBiI_4). In order to confirm the stability of the materials under investigation, PL spectra were measured for the compositions studied here (not including $x = 0$ for which no PL intensity was registered above background noise), under continuous illumination over 240 s in an inert nitrogen atmosphere. The PL spectra measured after 1, 60, 120, 180, and 240 s of illumination (at 41 W cm^{-2}) are shown in Figure S9, Supporting Information, and display small changes in intensity and no variation in spectral shape over 240 s of illumination, indicating the good stability of these materials under the experimental conditions employed in our study. All of the spectra peak between 1.58–1.70 eV, at substantial Stokes shifts of 300–400 meV from the band gap energy, with values of the full-width half-maxima all above 350 meV (see Figure S10b, Supporting Information).

The large Stokes shifts and FWHM observed for the PL are characteristic of strong electron–phonon couplings,[21,73] as has been observed for localized states in other silver-bismuth materials such as $\text{Cs}_2\text{AgBiBr}_6$,[23,26] $\text{Cu}_2\text{AgBiI}_6$[31,51] and $\text{Rb}_4\text{Ag}_2\text{BiBr}_9$.[7] Further, the PL band around 1.6–1.7 eV has been previously attributed to emission from a localized (small polaron) state in $\text{Cu}_2\text{AgBiI}_6$,[51] and we attribute the PL measured here to the formation of the same mechanism. We note that the energy of this band does not follow any clear trend with composition, indicating that the energetics of the localized state are independent of copper content, in good agreement with the small variation in band gap discussed above. The constant energy of this PL band serves as confirmation that the emission, and underlying localized state, is intrinsically associated with the presence of silver and bismuth in a close-packed iodide sublattice in these materials, and that the energy level of this state does not vary substantially, relative to the band structure, with composition.

To understand whether any variations in the energetics of the localized state occur over the first few nanoseconds of the PL decays, time-resolved emission spectra were also measured for the two most emissive compositions, $\text{Cu}_2\text{AgBiI}_6$ and $\text{Cu}_6\text{AgBiI}_{10}$, shown in **Figure 2**. The measurements reveal slightly differing behavior that provides insight into the trade-off between high-energy band-edge emission, around 2 eV (≈620 nm), and the localized-state emission around 1.7 eV (≈730 nm). For $\text{Cu}_2\text{AgBiI}_6$ (Figure 2a–c) some band-edge PL was measured between 600–650 nm over the first few nanoseconds, which decays more quickly than the main peak of the PL at around 730 nm. This is observed more clearly in the transient decays (Figure 2b), where the decays at 600 and 650 nm over the first ≈8 ns are somewhat faster than that at 730 nm, and also in the spectral slices shown in Figure 2c, where the high-energy band-edge PL disappears after the first ≈2 ns. In the case of $\text{Cu}_6\text{AgBiI}_{10}$ (Figure 2d–f), such band-edge emission is not observed, with transient decays at 600, 650, and 750 nm being generally very similar (Figure 2e) and little change apparent in the spectral slices taken over the first 10 ns (Figure 2f). Such change in the early-time PL spectra reveals that the ratio of band-edge PL to the highly Stokes-shifted PL arising from the small polaron is variable, and can be tuned by changing the quantity of Cu^+ versus Ag^+ and Bi^{3+}.

5. Observation of Ultrafast Charge-Carrier Localization and Small-Polaron Formation

To complete our understanding of the interactions between charges and the lattice in these silver-bismuth-halide materials, we carried out pump photon energy-dependent OPTP spectroscopy that gives insights into charge-carrier dynamics on a sub-picosecond timescale. OPTP spectroscopy measures the differential change in transmitted THz electric field, with and without photoexcitation, $-\Delta T/T$, which is directly proportional to the photoconductivity of a semiconductor, given by $\Delta\sigma = ne\mu$, where n is the photoexcited charge-carrier density and μ is the charge-carrier mobility.

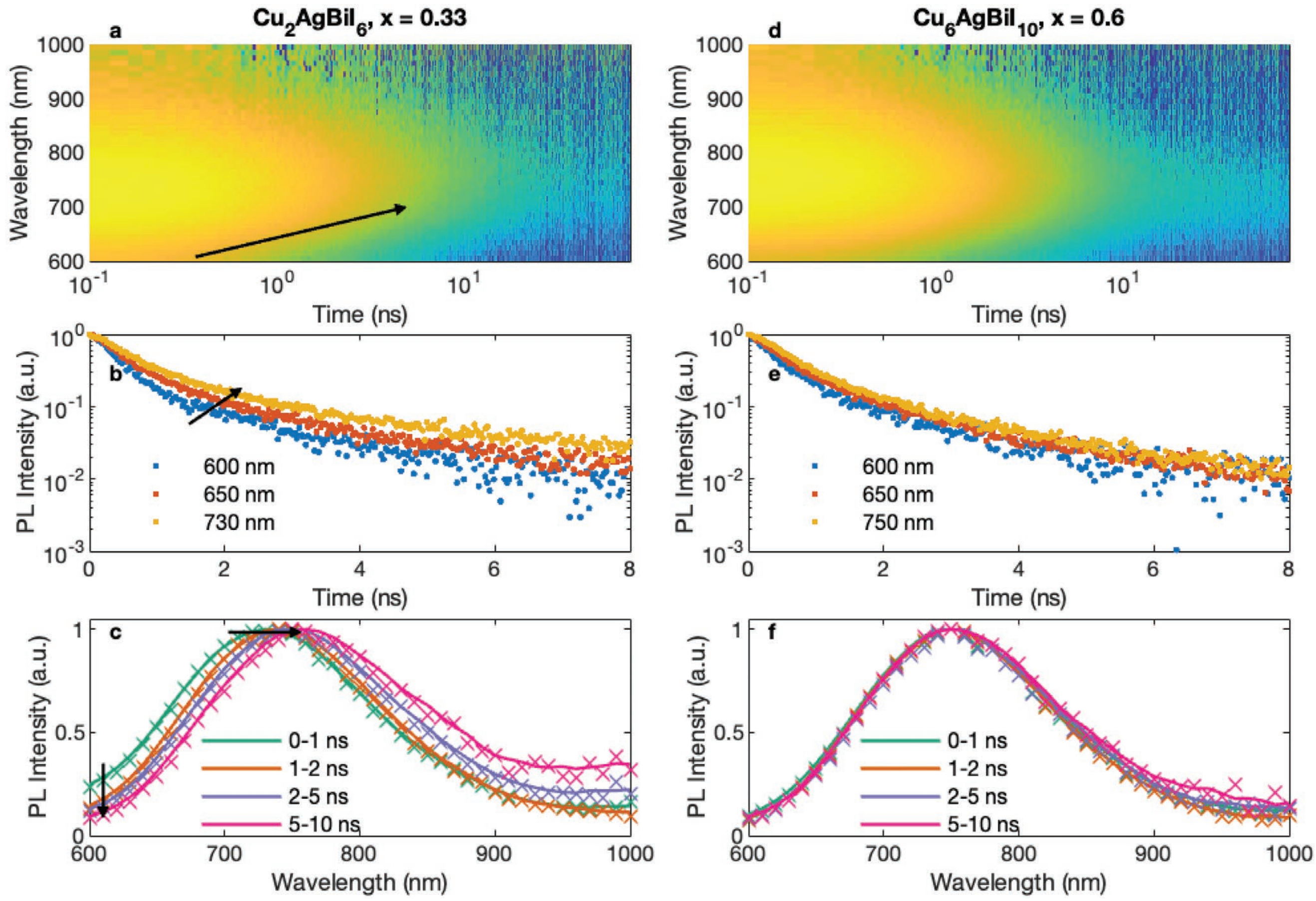

Figure 2. a) Time-resolved emission spectrum for a thin film of Cu_2AgBiI_6 ($x = 0.33$), measured at a fluence of 1610 nJcm^{-2}. b) Time-resolved PL decays at wavelengths of 550, 600, and 730 nm for Cu_2AgBiI_6 ($x = 0.33$), showing that the decay at higher energies (shorter wavelengths) is slightly faster than at the main PL peak at 730 nm. c) Time-resolved PL spectra for Cu_2AgBiI_6 ($x = 0.33$), integrated over different periods after photoexcitation, showing a red-shift in peak PL energy, as well as a drop in intensity of the high-energy PL over the first 10 ns. d) Time-resolved emission spectrum for a thin film of Cu_6AgBiI_{10} ($x = 0.6$), measured at a fluence of 1610 nJcm^{-2}. e) Time-resolved PL decays at wavelengths of 550, 600, and 750 nm for Cu_6AgBiI_{10} ($x = 0.6$), showing that the decay at higher energies (shorter wavelengths) is slightly faster than at the main PL peak at 750 nm, although less so than in the case of Cu_2AgBiI_6 ($x = 0.33$). f) Time-resolved PL spectra for Cu_6AgBiI_{10} ($x = 0.6$), showing very little change in PL spectral shape or peak energy over the first 10 ns.

The OPTP photoconductivity transients, shown in **Figure 3**, outline the dynamics of the charge-carrier localization that takes place in the silver-bismuth materials. The transients display an ultrafast decay in the photoconductivity over the first few picoseconds, with the signal decaying to close to zero for low x, whereas a substantial long-time conductivity remains for mid-to-high x values, in some cases over half of the initial peak in photoconductivity. These early-time dynamics over the first ≈6 ps, shows no dependence on fluence (Figure S16, Supporting Information), ruling out any influence from bi- or trimolecular recombination processes, such as exciton formation or Auger recombination. Instead, ultrafast photoconductivity decays similar to those observed in $Cu_{4x}(AgBi)_{1-x}I_4$ here, have previously been attributed to charge-carrier localization (i.e., the formation of small polarons) through temperature-dependent OPTP measurements for both $Cs_2AgBiBr_6$[23] and Cu_2AgBiI_6.[51] The fact that this decay is clearly present across all compositions investigated here, including for $x = 0$ (i.e., a composition with no copper), and also has been reported for the bromide-based double perovskite $Cs_2AgBiBr_6$, means that the charge-carrier localization is highly likely to derive from the presence of silver and/or bismuth in all of these materials. Further, the presence of such localization at pump energies of 2.1, 2.5, and 3.1 eV is strongly indicative of an intrinsic effect, and rules out any influences from a minority phase or impurity such as CuI, which has a band gap well above 2.1 eV.[58,59]

6. Unraveling the Sequence of Charge-Carrier Relaxation, Localization, and Recombination

Having examined the early-time charge-carrier localization process, we now proceed by examining the full charge-carrier dynamics, separating the OPTP photoconductivity transients into early- and long-time components in order to distinguish between different processes such as charge-carrier localization, trap-mediated and band-to-band recombination. **Figure 4**f schematically represents these processes, captured through fits to

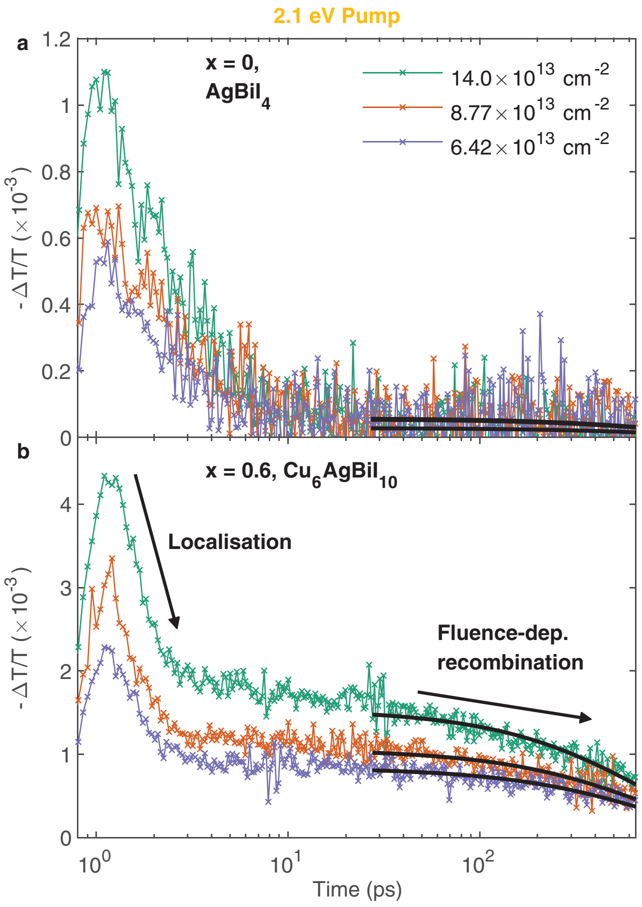

Figure 3. Photoconductivity transients over the first nanosecond after excitation, measured using OPTP spectroscopy, exciting at an energy of 2.1 eV (585 nm), for thin films with copper content a) $x = 0$ ($AgBiI_4$) and b) $x = 0.6$ (Cu_6AgBiI_{10}). Photoexcited charge carriers localize over the first few picoseconds, leading to the sharp drop in measured terahertz transmission $-\Delta T/T$, before recombining back to the ground state over longer timescales. For $AgBiI_4$ ($x = 0$) the photoconductivity decays to near-zero values within ≈10 ps, and the recombination over long timescales is fluence-independent. For (Cu_6AgBiI_{10} ($x = 0.6$) the photoconductivity after the first ≈5 ps remains substantial, and the long-time decays show a clear fluence dependence, indicating the presence of bimolecular (radiative) recombination. The black lines are fits to the decays beyond 25 ps, accounting for bimolecular radiative recombination and monomolecular trap-mediated recombination, as explained in the main text. The measurements were carried out with an incident photon flux of $N_A = 14.0$, 8.77, 6.42 × 10^{13} cm^{-2}. A full range of long-time photoconducticity transients following photoexcitation at 3.1, 2.5, and 2.1 eV (excess energies of 1.05, 0.45, and 0.05 eV) are shown in Figure S15, Supporting Information for all five compositions.

the early- and long-time dynamics that were carried out separately, given the distinctly different timescales for localization and recombination.

The early-time dynamics were fitted with a two-level mobility model that has previously been applied to temperature-dependent dynamics of $Cs_2AgBiBr_6$[23] and Cu_2AgBiI_6:[51] charge carriers are initially photoexcited into the conduction band into a free-carrier state with mobility μ_{deloc} and population n_{deloc}. Charge carriers then localise into a state with lowered mobility μ_{loc} and population n_{loc}, with the localization rate given by k_{loc}. The model is described in more detail in the Supporting Information, where we also provide the final expression that was fitted to the OPTP photoconductivity transients. These early-time fits were carried out between −2 and 8 ps globally across all fluences, for each composition and excitation wavelength. This approach allows for the extraction of values of k_{loc}, μ_{deloc} and μ_{loc} for each composition at excitation energies of 3.1, 2.5, and 2.1 eV.

Following localization, the photoconductivity dynamics are dominated by radiative and trap-mediated charge-carrier recombination processes occurring over longer timescales. To analyze these long-time dynamics, transients were fitted from 25 ps onward with the solution to an ordinary differential equation (ODE) that describes charge carriers recombining to the ground state via monomolecular (trap-mediated) and bimolecular (radiative) recombination, described by the following equation

$$n(t) = \frac{k_1 A}{e^{k_1 t} - A k_2} \tag{1}$$

Here, k_1 is the trap-mediated (monomolecular) recombination rate, k_2 is the radiative (bimolecular) recombination rate constant, and the constant A is defined such that $\frac{1}{A} = \frac{k_1}{n_0} + k_2$. We note that this type of ODE has been previously applied to describe the recombination of charge carriers in conventional metal-halide perovskites,[74,75] where photoexcited charge carriers take the form of large polarons,[21,43] as opposed to the small polarons that we identify with the long-time OPTP signal. However, given that the small polarons in silver-bismuth materials have reasonable charge-carrier mobilities at room temperature (see below and refs. [23] and [51]) and very low energy barriers to their temperature-activated motion,[23,51] and that exciton binding energies are relatively small, it is reasonable to assume that the dynamics of the localized state can be well described by the equation above. Fits were carried out for each composition and excitation energy of 3.1, 2.5, and 2.1 eV, globally across all fluences, yielding values of k_1 and k_2. We note that the fluence-dependence in the shape of the transients provides for the accurate extraction of the bimolecular rate constant k_2, as evident in Figure 3b and Figure S15, Supporting Information. However, in the case of $AgBiI_4$ ($x = 0$) the near-zero long-time OPTP signal and distinct lack of fluence dependence (Figure 3a) meant that a bimolecular recombination rate constant could not be extracted; these decays were therefore fitted with a monoexponential, and only a value of k_1 was obtained.

We begin discussion of the extracted parameters by examining trends in the values of the trap-mediated recombination rate k_1, shown in **Figure** 5a. Values obtained from fits to OPTP photoconductivity transients range between $k_1 = 10^8$–10^{10} s^{-1}, and are in excellent agreement with those extracted from the time-resolved PL measurements (shown as blue squares). These correspond to lifetimes around 0.1–10 ns, which is at the lower end of those typically encountered in lead-halide perovskites, but competitive with those for tin-rich tin-lead halide perovskites.[18] These values indicate a high density of traps and energetic disorder in all of the compositions, and follow no trend with pump excess energy, as would

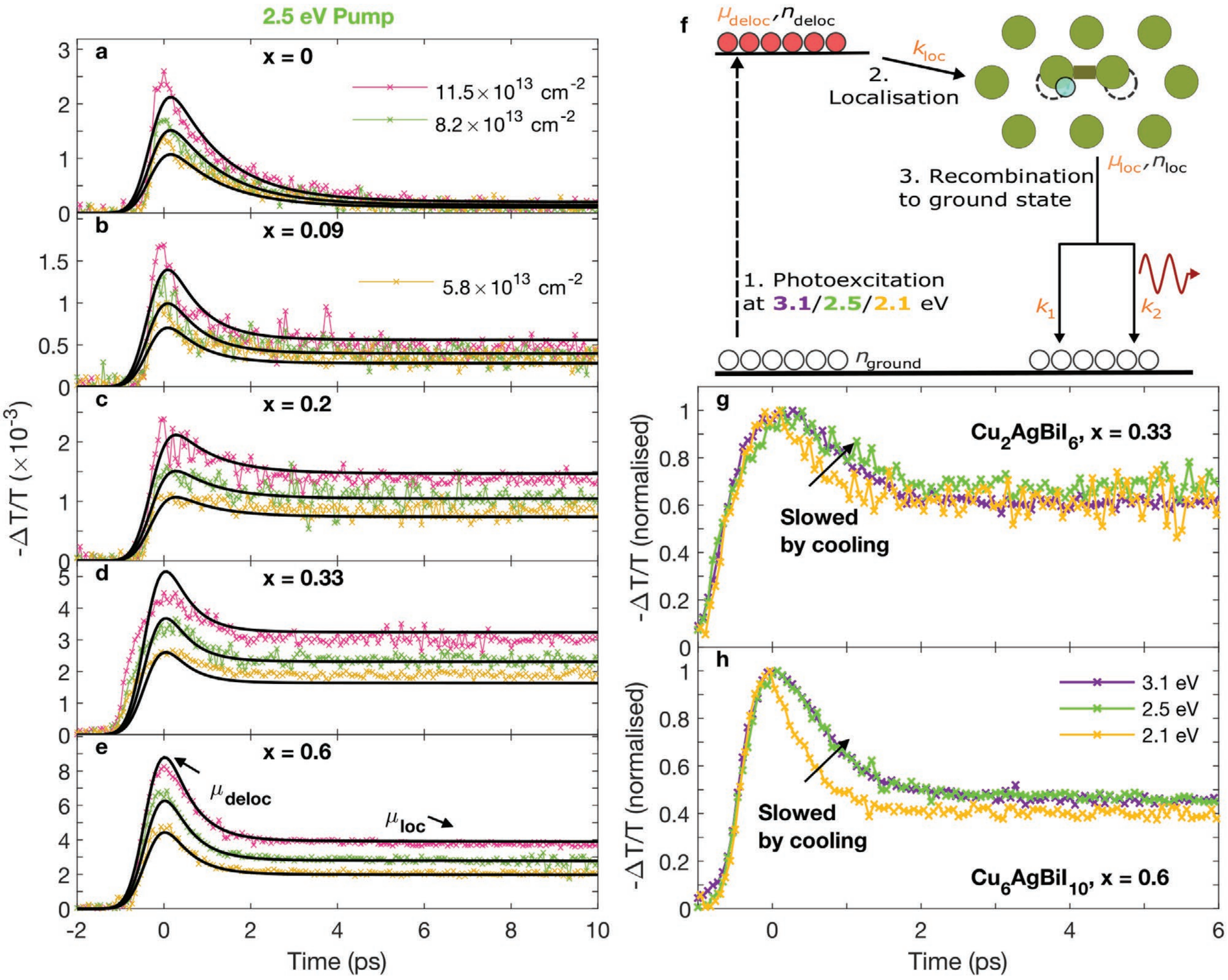

Figure 4. a–e) Fluence-dependent early-time photoconductivity transients for $Cu_{4x}(AgBi)_{1-x}I_4$, measured using OPTP spectroscopy with excitation at an energy of 2.5 eV (500 nm, excess energy of 0.45 eV above the bandgap). The black lines are fits to the decays between −2 and 8 ps using a two-level charge-carrier mobility model, explained in the main text. The initial peak amplitude determines the mobility μ_{deloc} of delocalized charge carriers, whereas the longer-time response is determined by the mobility μ_{loc} of localized charge carriers. Measurements were carried out with incident photon flux of $N_A = 11.5, 8.2, 5.8 \times 10^{13}cm^{-2}$. f) Schematic of the charge-carrier dynamic processes present across $Cu_{4x}(AgBi)_{1-x}I_4$. g,h) Normalized OPTP photoconductivity transients at times between −1–6 ps with respect to photoexcitation for thin films of g) $Cu_2(AgBi)I_6$ ($x = 0.2$) and h) $Cu_6(AgBi)I_{10}$ ($x = 0.6$), for photoexcitation at 3.1, 2.5, and 2.1 eV which generates charge-carrier densities of $n_0 = 1.50, 2.63, 1.96 \times 10^{18}cm^{-3}$ and $n_0 = 1.15, 1.26, 1.46 \times 10^{18}cm^{-3}$ for the two compositions, respectively (see Supporting Information for details). Transients obtained for excitation at photon energies of 3.1 and 2.5 eV decay more slowly over the first 1 ps than for excitation at 2.1 eV, indicating additional charge-carrier relaxing to the bottom of the band through thermalization and cooling. (Early-time transient decays following photoexcitation at 3.1 and 2.1 eV (excess energies of 1.05 and 0.05 eV) are shown for all five compositions in Figure S14, Supporting Information).

be expected for a monomolecular process: charge carriers relax, form small-polaron states and then diffuse to traps. The highest values of k_1, obtained for $AgBiI_4$ ($x = 0$), also correlate well with the absence of a detectable PL spectrum for that composition. Defect formation may be similar to that for the double perovskite $Cs_2AgBiBr_6$, where silver vacancies form easily and can act as localization centers for holes,[47,76] whilst a variety of other defect and vacancy states, including Bi vacancies and Bi_{Ag} antisites, can also act as charge-carrier trapping sites.[76,77] There is some disagreement in the literature on whether processing in a halide-poor, or a Bi-poor/halide-rich, environment would avoid the formation of such trap states.[76,77] Given the slight iodine deficiency identified in some of the films studied here, processing in a halide-rich environment may yield a reduction in defect density and improved charge-carrier transport, leading to enhanced device performance. By comparison, it has been shown that for metal-halide perovskites, charge-carrier lifetimes above hundreds of nanoseconds are desirable to reduce trap-mediated recombination and yield efficient current extraction and open-circuit voltage in an operating photovoltaic device.[2,78] Thus, the values of k_1 obtained here suggest that substantial improvements in materials processing and defect passivation may lead to highly efficient optoelectronic devices. Such work has shown great results for metal halide perovskites[79,80] but has been conducted on silver-bismuth semiconductors, such as $Cs_2AgBiBr_6$,[25] to a much lesser extent to date.

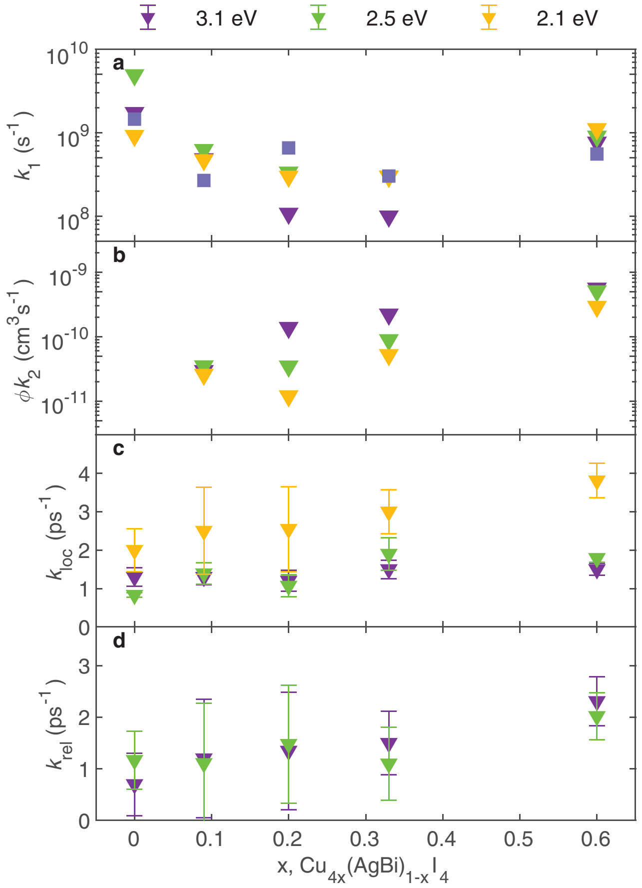

Figure 5. Charge-carrier rate constants obtained for $Cu_{4x}(AgBi)_{1-x}I_4$ thin films from fits to the long- and early-time OPTP photoconductivity transients, plotted versus Cu^+ content x. Parameters are shown in purple, green and yellow according to the used photoexcitation energies of 3.1, 2.5, and 2.1 eV, respectively. a) Monomolecular (trap-mediated) recombination rate constant k_1 obtained from fits to the long-time OPTP data. The blue squares are values of k_1 obtained from fits to the PL decays recorded by TCSPC (see SI for details), which are in excellent agreement with those extracted from the OPTP measurements. b) Effective bimolecular (radiative) recombination rate constant ϕk_2 obtained from fits to the long-time OPTP transients. The bimolecular rate constant is enhanced with higher x (increasing Cu^+ content), in good agreement with the increased measured PL intensities. c) Localization rate k_{loc} obtained from fits to the early-time OPTP transients. The localization rate is slightly larger for increasing x, and is also markedly larger when films are photoexcited near resonance at 2.1 eV, as opposed to higher up into the bands at 2.5 or 3.1 eV. d) Extracted charge-carrier relaxation rate k_{rel}, obtained from the difference between the localization rates at 2.5 and 3.1 eV and the localization rate at 2.1 eV for each composition.

We continue by discussing the mechanisms for radiative bimolecular (band-to-band) recombination in $Cu_{4x}(AgBi)_{1-x}I_4$. We note that OPTP photoconductivity spectroscopy yields only an effective bimolecular radiative recombination rate constant, ϕk_2, where ϕ is the branching ratio of absorbed photons to free charge carriers generated. Given that the exciton binding energies are comparable to thermal energies at room temperatures, ϕ may be somewhat smaller than 1, in particularly for compositions with small x. Values of ϕk_2, shown in Figure 5b, increase markedly with x, rising from a value of $\approx 0.3\times10^{-10}$ cm^{3}s^{-1} for $x = 0.09$ up to $\approx 6\times10^{-10}$ cm^{3}s^{-1} for $x = 0.6$, correlating well with the increased intensity observed in the steady-state PL measurements and with the enhanced film roughness, which would increase light out-coupling from the thin films.[81,82] We also observe an increase in value of ϕk_2 with pump excess energy, seen across all compositions. We attribute this to an increase in the photon-to-charge branching ratio ϕ: as the pump energy increases well above the band gap, fewer excitons are formed following the initial photoexcitation, leading to increased electron–hole radiative recombination.

For conventional lead-halide perovskites, radiative band-to-band recombination has been shown to be the inverse of optical absorption.[83] However, examining correlations between band-edge absorption strength shown in Figure 1e and bimolecular recombination rates shown in Figure 5b, we find that this principle does not appear to apply to the small-polaron localized state in $Cu_{4x}(AgBi)_{1-x}I_4$. Instead, we observe the opposite trend to that expected from the principle of detailed balance: ϕk_2 rises and $\alpha_{2.3}$ falls with increasing x, and the ratio of $\frac{\phi k_2}{\alpha_{2.3}}$ rises by two orders of magnitude across the compositional range, rather than remaining constant. This observation cannot be caused by variations in refractive index, as the dielectric constants show little trend with x (as shown in Figure 1g and discussed in Section S6, Supporting Information). In addition, given the similarity in exciton binding energies across the compositional range, the photon-to-charge branching ratio ϕ should not change to such an extreme extent, and neither would surface roughness. Instead, we suggest that some of the assumptions around the principle of detailed balance calculations (which leads to the conclusion that bimolecular recombination is the inverse of optical absorption[83]) no longer apply to radiative recombination from a small polaron state. Indeed, Wu et al. argue that polaron formation in $Cs_2AgBiBr_6$ allows for much larger bimolecular recombination rate constants than would be expected for this indirect gap semiconductor, as charge-carrier localization leads to a breakdown of the band-to-band recombination picture.[45]

As an alternative description, we may consider the Langevin model for radiative recombination, often applied to organic semiconductors that typically support small polarons.[84] The Langevin model assumes that electron–hole recombination proceeds through charge capture into the Coulomb potential generated by the opposite charge, making bimolecular recombination rates proportional to the approach velocity and therefore mobility of the charge carrier. In this simple model, the radiative rate constant is therefore determined by $k_2^{\text{Langevin}} = e\mu/\varepsilon_0\varepsilon_r$. Using an approximate average value determined here for the small polaron mobility $\mu_{\text{loc}} \approx 1\,\text{cm}^2\,\text{V}^{-1}\,\text{s}^{-1}$ (see below) and $\varepsilon_r = \varepsilon_\infty^{\text{THz}} \approx 6$ yields $k_2^{\text{Langevin}} \approx 3\times10^{-7}$ cm^{3}s^{-1}, several orders of magnitude above what is found here across the entire compositional range. Therefore the Langevin criterion does not appear to be quantitatively satisfied at first sight. However, the strong correlation between the bimolecular recombination rate constants and the charge-carrier mobilities (discussed below) across the compositional series qualitatively support the notion of Langevin-like recombination. One potential explanation for the numeric discrepancy is that the charge-carrier localization observed here may only affect one species, reducing the charge-carrier mobility for that species but leaving a reasonably high mobility for the remaining free carrier in a large polaron state. In such a scenario, for which the mobility of one species is much larger than that of the other, Monte-Carlo-based simulations of organic polymer blends have shown that bimolecular recombination can be somewhat below the Langevin limit, depending on the precise ratio of charge-carrier mobilities.[85] Although the situation for an inorganic crystalline semiconductor is somewhat different, with long-range order and higher charge-carrier mobilities, a similar underlying principle may apply, leading to charge-carrier recombination rates for small polarons in silver-bismuth materials that are qualitatively well-described by a Langevin-type model, whilst remaining numerically somewhat below the Langevin limit.

We further analyze the charge-carrier localization rate k_{loc} in order to understand how compositional variations impact the localization process, and we find two interesting trends in the fitted values (see Figure 5c). First, the localization rate increases slightly with x (increasing $\mathrm{Cu^+}$ content), for all pump wavelengths. We attribute this to a slight change in the crystal structure of the materials as $\mathrm{Cu^+}$ content increases: as we note above, materials with high copper content such as $\mathrm{Cu_2AgBiI_6}$ have a layered 2D octahedral network,[31] whereas $\mathrm{AgBiI_4}$ has been shown to have octahedral networks that are fully connected in all three dimensions.[27,62] Given that charge-carrier localization has been shown to depend on the dimension of a system,[21,73,86,87] with lower-dimensional systems having faster localization with lower or nonexistent energetic barriers, this finding agrees well with the theoretical predictions. However, we note that the effect is quite small, that is, we do not see an order-of-magnitude change in localization rate, and this could be linked to the general low electronic dimensionality of silver-bismuth materials,[21,55,88] which might dominate over any changes in structural dimensionality.

Second, we find that the localization rate is much larger, nearly doubled, when photoexcitation occurs near resonance at 2.1 eV, as opposed to higher up into the bands at 3.1 or 2.5 eV (excess energies of 1.05 and 0.45 eV, respectively). We attribute this to charge-carrier relaxation preceding localization, when photoexcitation occurs well above the band gap. Studies of conventional metal-halide perovskites using OPTP spectroscopy have found slower rises in photoconductivity with increasing pump energy,[89,90] attributed to charge-carrier relaxation occurring within the first hundreds of femtoseconds: as relaxation to the bottom of the band takes place, the charge-carrier mobility increases because the band extrema are more highly curved, leading to a rise in photoconductivity response over the relaxation timescale. Such a pronounced rise in mobility (and thus photoconductivity) over the first few hundred femtoseconds is not observed in the silver-bismuth materials studied here, most likely because of the very flat band structure found in such materials,[6,91] which would lead to little change in mobility as carriers relax. Thus, the photoconductivity dynamics observed for the silver-bismuth materials in this study suggest that charge carriers must first relax to the bottom of the band and lose significant energy before effectively being able to localize into a small polaron state. We thus obtain more accurate values for the rate for localization by generating charge carriers close to the band gap at 2.1 eV, leading to negligible initial charge-carrier relaxation, which yields a localization rate between $2-4\ \mathrm{ps^{-1}}$ ($\tau_{\mathrm{loc}} \approx 0.25$–$0.5$ ps). Instead, when photoexcition occurs above resonance at 3.1 and 2.5 eV, charge carriers must first undergo relaxation via both thermalization and charge-carrier cooling[89,92–94] before localizing to the small polaron state (as shown in Figure 4g,h). In order to quantify the timescale of charge-carrier relaxation, we calculate $k_{\mathrm{rel}} = k_{\mathrm{loc}}^{2.1\mathrm{eV}} - k_{\mathrm{loc}}^{3.1\mathrm{or}2.5\mathrm{eV}}$, which yields rough estimates around $1-2\ \mathrm{ps^{-1}}$ ($\tau_{\mathrm{rel}} \approx 0.5$–$1$ ps), in good agreement with timescales between 0.1–1 ps for charge-carrier relaxation found in conventional lead-halide perovskites.[89,94]

Overall, our analysis of the photoconductivity transients provides clear insights into the dynamical charge-carrier processes occurring in the silver-bismuth semiconductors $\mathrm{Cu}_{4x}(\mathrm{AgBi})_{1-x}\mathrm{I}_4$ from sub-picosecond through to nanosecond timescales. When photoexcitation occurs above resonance charge carriers first relax to the bottom of the conduction band over the first 0.5–1 ps. Charge carriers are photoexcited into a free-carrier (delocalized) large-polaron state and, once cooled, localise over the next 0.25–0.5 ps into a small polaron state. Such small polarons subsequently recombine, through either trap mediated recombination over a nanosecond time scale, or through fluence-dependent radiative bimolecular recombination that gives rise to the highly Stokes-shifted photoluminescence at energies around 1.6–1.7 eV. An assessment across the compositional series reveals that the replacement of $\mathrm{Ag^+}$ and $\mathrm{Bi^{3+}}$ with $\mathrm{Cu^+}$ increases the rates of both charge-carrier relaxation and localization—a direct consequence of the enhanced curvature at the valence band maximum with increased contributions from copper electronic states, as well as the shift from a 3D to a 2D octahedral network, as discussed above. In addition, the radiative bimolecular recombination rate constants are found to increase with $\mathrm{Cu^+}$ content, in good agreement with the enhanced PL signal. However, the mechanism of bimolecular recombination in these materials is found to deviate from that observed in conventional metal halide perovskites. The anticorrelation between bimolecular rates constants and strength of absorption near the band edge indicate that the detailed-balanced approach described by Davies et al.[83] does not apply to these silver-bismuth materials. Instead the correlation between bimolecular rate constants and charge-carrier mobilities suggests that radiative recombination from the small polaron state may take place via a Langevin-style process.

7. Influence of $\mathrm{Cu^+}$ on Charge-Carrier Mobility and Transport Mechanism

To gain insights into charge-carrier transport in $\mathrm{Cu}_{4x}(\mathrm{AgBi})_{1-x}\mathrm{I}_4$ semiconductors and how it may be affected by charge-carrier localization, we present in **Figure 6** the values of the effective charge-carrier mobilities extracted from the fits to the early-time OPTP dynamics. Again, these values combine the "true" mobilities of the large/small polaron states (μ_{deloc} and μ_{loc}, respectively) with the photon-to-charge branching ratio ϕ, which may vary as the pump excess energy is altered. We further note that OPTP spectroscopy is only able to probe directly the sum charge-carrier mobility arising from

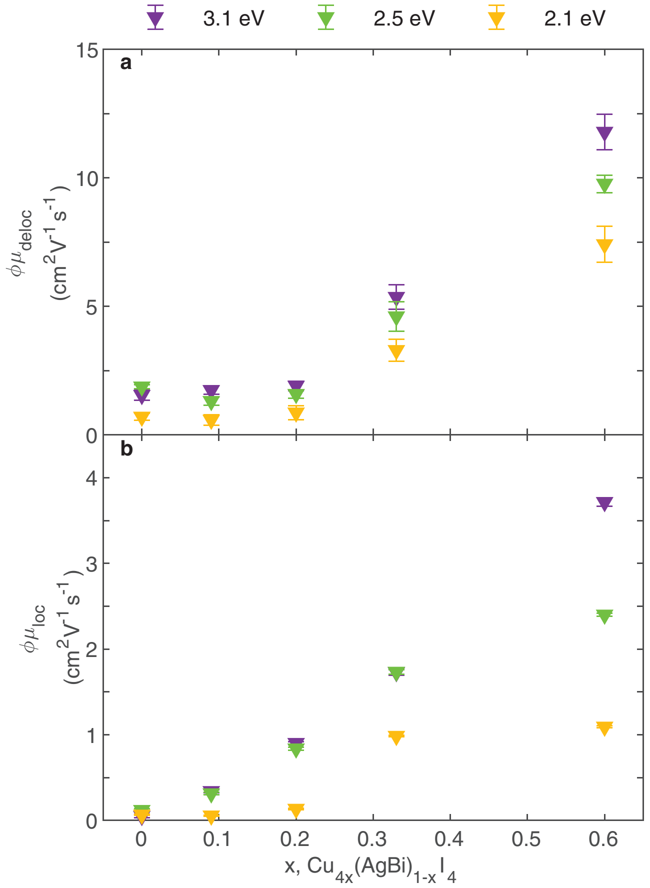

Figure 6. Effective electron-hole sum mobilities for $Cu_{4x}(AgBi)_{1-x}I_4$ thin films obtained from fits to the early-time OPTP photoconductivity transients and plotted versus Cu^+ content x. Values are shown in purple, green, and yellow according to the used photoexcitation energies of 3.1, 2.5, and 2.1 eV, respectively. a) Effective large-polaron mobility $\phi\mu_{\text{deloc}}$ and b) effective small polaron mobility $\phi\mu_{\text{loc}}$. Values increase markedly with x because of reduced charge-carrier effective masses, and also rise with increasing pump excess energy because of increases in free-charge-to-photon branching ratios by which the mobility values are factored.

contributions from both electrons and holes; $\mu_{\text{deloc/loc}}$ thus represent the total sum mobility for the electrons and holes in the large and small polaron states, respectively. The values of the effective large polaron mobility $\phi\mu_{\text{deloc}}$ show two clear trends: a sharp increase in charge-carrier mobility with x, from 1.5 to 11.7 cm^2 V^{-1} s^{-1} (a trend observed across all three photoexcitation energies); and rising values of $\phi\mu_{\text{deloc}}$ with increasing pump excess energy.

The increase in large polaron mobility with x is likely caused by several complementary effects: charge-carrier mobilities depend on a mix of intrinsic factors, such as charge-lattice couplings or local electronic band structure, and extrinsic factors such as scattering off grain boundaries or local fluctuations in the energy landscape.[74,95] As is clear from the steady-state PL measurements, increased Cu^+ presence leads to some reduction in trap density and energetic disorder, reducing scattering from defects and improving charge-carrier mobilities. Further, although a transition from a 3D to a 2D octahedral network occurs with increasing x, this effect is countered somewhat by the accompanying increase in tetrahedrally-coordinated Cu^+ improving general electronic connectivity, as argued above, which aids charge transport. Finally, as mentioned above, DFT calculations carried out on both $CuBiI_4$[64] and Cu_2AgBiI_6[31] have shown substantial contributions to the valence band maximum from Cu-d electronic states (as opposed to from Ag-d and Bi-s states in $Cs_2AgBiBr_6$[70,91,96]). We suggest that increased relative contributions from copper states leads to a more strongly curved valence band maxima,[70,91,96] and correspondingly higher mobilities and lower effective masses for holes.

We attribute the trend of increasing value of $\phi\mu_{\text{deloc}}$ with increasing pump excess energy for any given composition to a rise in photon-to-charge branching ratio ϕ: as the pump excess energy rises well above the band gap, fewer neutral excitons and more free charge carriers are formed.[97,98] Given that only individual electrons or holes contribute to the measured THz photoconductivity in the energy range studied here, and that neutral excitons do not (as $E_B > 10$ meV), an increase in the proportion of free charges being formed, relative to excitons, will be registered as a larger $-\Delta T/T$ signal and subsequently higher charge-carrier mobility. Similar trends have been observed through time-resolved microwave conductivity on $MAPbI_3$.[97] An alternative explanation for this trend is that the increased charge-carrier mobility with increasing pump excess energy is linked to probing different locations of the band structure. However, given that higher-lying bands in silver-bismuth materials tend to be flatter than the band extrema,[65,91,96] we would expect the opposite trend to that observed here, that is, decreased values of μ_{deloc} with increasing pump excess energy and therefore rule out this explanation.

The effective mobility of the small polaron state, $\phi\mu_{\text{loc}}$, follows similar trends to those observed for the large polaron mobility: it increases sharply with x and also increases with pump excess energy, for analogous reasons. The trend of higher mobility values with x implies a reduced "barrier" to the hopping-type transport typical of small polarons.[48,73] This may appear contradictory to the observed rise in localization rate k_{loc} with increasing x, but the two processes are physically distinct: the localization rate is a proxy for the size of the energetic barrier between delocalized and localized states in a material,[86] whereas the small polaron mobility gives an indication of the energetic barrier for movement of a localized charge from one particular lattice site to another.[48] Thus, the enhanced electronic connectivity that follows increased Cu^+ content leads to higher small polaron mobilities; most likely because the spatial separation between electronic states arising from Ag^+ and Bi^{3+} octahedra,[55,56] is lowered, which in turn reduces the barrier to charge motion. Alternatively, studies of a variety of silver-bismuth materials have argued for selective localization of holes on Ag^+ sites or electrons on Bi^{3+} sites.[30,47] Given that our two-level mobility model, for simplicity, does not assume contributions from distinct electrons and holes, this observed rise in μ_{loc} could also be interpreted as an increased mobility of the remaining, non-localized, free charges. Thus, one photoexcited species (e.g., electrons) could localise very rapidly, reducing the measured photoconductivity, but the other remains free to move, contributing to the photoconductivity well beyond the first few picoseconds. We note that the substantial rise in charge-carrier mobility with increasing Cu^+ content makes these materials the most promising for implementation in photovoltaic devices. In particular, $Cu_{4x}(AgBi)_{1-x}I_4$ with $x = 0.2$ and above shows good charge-carrier mobilities of $\approx 1\ cm^2\ V^{-1}\ s^{-1}$ or more at long timescales for which small polarons have formed, which are most relevant to charge-carrier extraction. For $AgBiI_4$, on the other hand, small polaron formation leads to negligible remnant charge-carrier mobility, making such AgBi-rich, Cu-poor materials less suitable for photovoltaic applications.

8. Understanding, Mitigating, and Tailoring Charge-Carrier Localization

Overall, in this work we have shown that small polaron formation takes place across the compositional series $Cu_{4x}(AgBi)_{1-x}I_4$, regardless of changes in crystal structure with Cu^+ content, implying such localization is intrinsically linked to the presence of Ag^+ and Bi^{3+}. Importantly, such localization effects can be adapted and mitigated by variations in the crystal structure (between a 2D and 3D octahedral network), and by dilution of the amount of Ag^+ and Bi^{3+}, relative to Cu^+, allowing for greater electronic conductivity. As we have shown, Cu^+ addition can tailor charge-carrier dynamics and transport, both of which are crucial for determining suitability across a variety of optoelectronic applications. We find that such charge-carrier localization also leads to a modification of band-to-band bimolecular recombination mechanisms, typically described by a radiative-balance approach for lead halide perovskites, but for small polarons in $Cu_{4x}(AgBi)_{1-x}I_4$ more akin to Langevin-type recombination, similar to processes in organic semiconductors. Further, we have shown that enhanced Cu^+ content leads to a reduction in charge-carrier effective masses and increased charge-carrier mobilities, linked to the increased contributions of copper electronic states at the valence band maximum. We end this section with a discussion of attempted strategies for the alteration of localization effects across wider material classes, focusing on the influence of chemical composition, electronic dimensionality and structural distortion[21] with a view of guiding further materials development.

Compositional tuning through use of mono- and tri-valent alternatives to silver and bismuth has been explored for a range of semiconductors,[8,65] by substitution of Na^+,[99] K^+, Tl^+, or In^+ for Ag^+, and Tl^{3+},[100] Sb^{3+}[70,101,102] or In^{3+}[102,103] for Bi^{3+}. Substitution of Na^+ for Ag^+ in $Cs_2Ag_{1-y}Na_yBiCl_6$ has been shown to lead to local structural distortions deriving from mismatched octahedra for large doping levels ($y > 0.6$);[99] combined with the predicted low electronic dimensionality of $Cs_2NaBiCl_6$,[55,65] this could imply a similar or stronger amount of charge-carrier localization, relative to the silver-based material.

With regards to substitutions of bismuth, attempted doping of $Cs_2AgBi_{1-y}In_yBr_6$ with In^{3+} has had very limited success in photovoltaic devices,[103] and the increased emission with indium content from the highly Stokes-shifted main PL band correlates well with its assignment to a localized state, possibly also implying stronger charge-carrier localization.[23,26,47] Further, for the indium-based material $Cs_2AgInCl_6$ it has been suggested that holes localise on $[AgCl_6]$ octahedra, leading to the formation of self-trapped excitons that result in broad, highly Stokes-shifted emission.[3,104] Based on such initial results, we would thus not recommend applying such substitutions to the series of silver-bismuth materials investigated here. Recent theoretical work on the double perovskites $Cs_2Ag(Bi/Sb)X_6$ ($X = Br^-$, Cl^-) by Biega et al.[70] has suggested that swapping Bi^{3+} for Sb^{3+} leads to somewhat reduced exciton localization (without removing it entirely).[70] Separately, studies of BiI_3,[35] $(MA)_3Bi_2I_9$,[36] and $(MA)_3Sb_2I_9$[57] by Scholz et al. have found very strong electron–phonon couplings across all of these materials, confirming that the observed charge-carrier localization is linked intimately to the presence of bismuth or antimony, rather than the specifics of a particular crystal structure. This finding is in excellent agreement with our observation that structural and compositional variations across the solid solution line alter, but do not completely remove, charge-carrier localization.

To examine the specific impact of crystal structure on charge-carrier localization, alterations to the structural dimension of silver-bismuth materials can be attempted. This approach has been pursued for layered Ruddlesden–Popper versions of the double perovskite $Cs_2AgBiBr_6$,[29] where a reduction from two to one octahedral layers facilitated structural distortions that are likely to aid charge-carrier localization. Another, similar approach is to design tailored large organic spacer cations that can separate individual sub-units of the crystal sub-structure, which had been implemented for $(AE2T)_2AgBiI_8$.[30] Through variation of the length and dipolar nature of such organic cations, the "stiffness" of the lattice could be reduced or enhanced, depending on the application, allowing for a variation in strength of electron–phonon coupling.[21] However, given that charge-carrier localization in $Cu_{4x}(AgBi)_{1-x}I_4$ studied here is linked closely to the presence of bismuth and silver, owing to the large electronegativity of the silver- and bismuth-halide bonds and the structural instability of bismuth, such structural variation is likely to provide an avenue for tailoring, rather than entirely removing, charge-carrier localization in these materials.

Overall, these examples show that compositional substitution can provide an effective tool for removing or reducing charge-carrier localization in metal halide semiconductors. While replacement of Ag^+ with Na^+ and of Bi^{3+} with Sb^{3+} has not appeared to be fully successful in early studies, it is clear that such investigations are at an incipient stage. Future studies that examine the influence of specific compositional replacements for silver and bismuth, or of structural alterations, on charge-carrier localization will help to unlock the potential of silver-bismuth semiconductors across a wide range of optoelectronic applications. Given that these materials have to date received significantly less attention and research focus compared to their more prominent lead halide perovskites counterparts, such research is likely to form a highly promising future avenue toward lead-free materials for photovoltaic applications.

9. Conclusion

In conclusion, we have demonstrated the promise of new quaternary Cu-Ag-Bi-I semiconductors, $Cu_{4x}(AgBi)_{1-x}I_4$, that have direct band gaps in the visible range, low exciton binding energies, and good charge-carrier mobilities rising to above 10 $cm^2V^{-1}s^{-1}$ for high Cu^+ content. We find that the addition of Cu^+ markedly improves general optoelectronic properties by reducing disorder and improving general electronic connectivity throughout the lattice, enhancing PL emission and charge-carrier transport, which is highly favorable for both light emission and photovoltaic applications. Through excess-energy dependent OPTP spectroscopy, we are able to unravel the dynamics of charge carriers relaxing and localizing from large- to small-polaron states on a sub-picosecond time scale, and subsequently recombining through trap-mediated and radiative bimolecular recombination. We show that for these silver-bismuth materials, the principle of detailed balance fails to describe band-to-band recombination of small polarons adequately. Instead, correlation between charge-carrier mobilities and bimolecular recombination constants across the series suggest that such processes may be better described by the Langevin model. Further, increased Cu^+ content leads to reduced exciton binding energies and enhanced charge-carrier mobilities, which we link to a reduction in charge-carrier effective masses caused by enhanced contributions from copper states at the VBM. Overall, $Cu_{4x}(AgBi)_{1-x}I_4$ semiconductors with higher Cu^+ appear to display the most advantageous optoelectronic properties in this series, since, despite their faster localization dynamics, they display the highest small-polaron mobilities and strongest radiative recombination. We thus conclude that although charge-carrier localization takes place across Ag^+ and Bi^{3+} containing compositions across the solid solution line of $AgBiI_4$–CuI and is most likely linked to the presence of Ag^+ and Bi^{3+}, its impact can be tailored and mitigated by changes in crystal structure and electronic connectivity, opening a new window into material design for optoelectronic applications.

Supporting Information

Supporting Information is available from the Wiley Online Library or from the author.

Acknowledgements

The authors are thankful to the Engineering and Physical Sciences Research Council (EPSRC) for financial support. L.R.V.B acknowledges funding from the EPSRC Centre for Doctoral Training in New and Sustainable Photovoltaics and the Oxford-Radcliffe Scholarship. L.M.H thanks TUM-IAS for a Hans Fischer Senior Fellowship. H.C.S. acknowledges funding from the EPSRC Prosperity Partnership EP/S004947/1. A.M.U. thanks the EPSRC Centre for Doctoral Training in Plastic Electronics for financial support through a graduate scholarship.

Conflict of Interest

The authors declare no conflict of interest.

Data Availability Statement

The data that support the findings of this study are available from the corresponding author upon reasonable request.

Keywords

charge-carrier localization, perovskites, polarons, silver-bismuth-halides, spectroscopy

Received: September 9, 2021
Revised: October 8, 2021

[1] M. A. Green, A. Ho-Baillie, H. J. Snaith, *Nat. Photonics* **2014**, *8*, 506.
[2] M. B. Johnston, L. M. Herz, *Acc. Chem. Res.* **2016**, *49*, 146.
[3] J. Luo, X. Wang, S. Li, J. Liu, Y. Guo, G. Niu, L. Yao, Y. Fu, L. Gao, Q. Dong, C. Zhao, M. Leng, F. Ma, W. Liang, L. Wang, S. Jin, J. Han, L. Zhang, J. Etheridge, J. Wang, Y. Yan, E. H. Sargent, J. Tang, *Nature* **2018**, *563*, 541.
[4] C. Zhou, Y. Tian, Z. Yuan, H. Lin, B. Chen, R. Clark, T. Dilbeck, Y. Zhou, J. Hurley, J. Neu, T. Besara, T. Siegrist, P. Djurovich, B. Ma, *ACS Appl. Mater. Interfaces* **2017**, *9*, 44579.
[5] Best Research-Cell Efficiency Chart | Photovoltaic Research | NREL, https://www.nrel.gov/pv/cell-efficiency.html (accessed: Feb 2021)
[6] A. H. Slavney, T. Hu, A. M. Lindenberg, H. I. Karunadasa, *J. Am. Chem. Soc.* **2016**, *7*, 2138.
[7] M. Sharma, A. Yangui, V. R. Whiteside, I. R. Sellers, D. Han, S. Chen, M.-H. Du, B. Saparov, *Inorg. Chem.* **2019**, *58*, 4446.
[8] F. Giustino, H. J. Snaith, *ACS Energy Lett.* **2016**, *1*, 1233.
[9] C. C. Boyd, R. Cheacharoen, T. Leijtens, M. D. McGehee, *Chem. Rev.* **2019**, *119*, 3418.
[10] E. T. Hoke, D. J. Slotcavage, E. R. Dohner, A. R. Bowring, H. I. Karunadasa, M. D. McGehee, *Chem. Sci.* **2015**, *6*, 613.
[11] A. J. Knight, A. D. Wright, J. B. Patel, D. P. McMeekin, H. J. Snaith, M. B. Johnston, L. M. Herz, *ACS Energy Lett.* **2018**, *4*, 75.
[12] B. Conings, J. Drijkoningen, N. Gauquelin, A. Babayigit, J. D'Haen, L. D'Olieslaeger, A. Ethirajan, J. Verbeeck, J. Manca, E. Mosconi, F. D. Angelis, H. G. Boyen, *Adv. Energy Mater.* **2015**, *5*, 1500477.
[13] G. Flora, D. Gupta, A. Tiwari, *Interdiscip. Toxicol.* **2012**, *5*, 47.
[14] C. C. Stoumpos, C. D. Malliakas, M. G. Kanatzidis, *Inorg. Chem.* **2013**, *15*, 9019.
[15] N. K. Noel, S. D. Stranks, A. Abate, C. Wehrenfennig, S. Guarnera, A.-A. Haghighirad, A. Sadhanala, G. E. Eperon, S. K. Pathak, M. B. Johnston, A. Petrozza, L. M. Herz, H. J. Snaith, *Energy Environ. Sci.* **2014**, *9*, 3061.
[16] E. S. Parrott, T. Green, R. L. Milot, M. B. Johnston, H. J. Snaith, L. M. Herz, *Adv. Funct. Mater.* **2018**, *28*, 1802803.
[17] R. L. Milot, M. T. Klug, C. L. Davies, Z. Wang, H. Kraus, H. J. Snaith, M. B. Johnston, L. M. Herz, *Adv. Mater.* **2018**, *30*, 1804506.
[18] K. J. Savill, A. M. Ulatowski, L. M. Herz, *ACS Energy Lett.* **2021**, *13*, 2413.
[19] M. R. Filip, F. Giustino, *Proc. Natl. Acad. Sci. USA* **2018**, *115*, 5397.
[20] G. Volonakis, M. R. Filip, A. A. Haghighirad, N. Sakai, B. Wenger, H. J. Snaith, F. Giustino, *J. Phys. Chem. Lett.* **2016**, *7*, 1254.
[21] L. R. V. Buizza, L. M. Herz, *Adv. Mater.* **2021**, *33*, 2007057.
[22] L. Schade, A. D. Wright, R. D. Johnson, M. Dollmann, B. Wenger, P. K. Nayak, D. Prabhakaran, L. M. Herz, R. Nicholas, H. J. Snaith, P. G. Radaelli, *ACS Energy Lett.* **2019**, *1*, 299.
[23] A. D. Wright, L. R. V. Buizza, K. J. Savill, G. Longo, H. J. Snaith, M. B. Johnston, L. M. Herz, *J. Phys. Chem. Lett.* **2021**, *12*, 3352.
[24] B. Wang, N. Li, L. Yang, C. Dall'agnese, A. K. Jena, S. I. Sasaki, T. Miyasaka, H. Tamiaki, X. F. Wang, *J. Am. Chem. Soc.* **2021**, *143*, 2207.
[25] G. Longo, S. Mahesh, L. R. V. Buizza, A. D. Wright, A. J. Ramadan, M. Abdi-Jalebi, P. K. Nayak, L. M. Herz, H. J. Snaith, *ACS Energy Lett.* **2020**, *5*, 2200.

[26] S. J. Zelewski, J. M. Urban, A. Surrente, D. K. Maude, A. Kuc, L. Schade, R. D. Johnson, M. Dollmann, P. K. Nayak, H. J. Snaith, P. Radaelli, R. Kudrawiec, R. J. Nicholas, P. Plochocka, M. Baranowski, *J. Mater. Chem. C* **2019**, *7*, 8350.
[27] H. C. Sansom, G. F. Whitehead, M. S. Dyer, M. Zanella, T. D. Manning, M. J. Pitcher, T. J. Whittles, V. R. Dhanak, J. Alaria, J. B. Claridge, M. J. Rosseinsky, *Chem. Mater.* **2017**, *29*, 1538.
[28] A. Koedtruad, M. Goto, M. A. Patino, Z. Tan, H. Guo, T. Nakamura, T. Handa, W. T. Chen, Y. C. Chuang, H. S. Sheu, T. Saito, D. Kan, Y. Kanemitsu, A. Wakamiya, Y. Shimakawa, *J. Mater. Chem. A* **2019**, *7*, 5583.
[29] B. A. Connor, L. Leppert, M. D. Smith, J. B. Neaton, H. I. Karunadasa, *J. Am. Chem. Soc.* **2018**, *140*, 5235.
[30] M. K. Jana, S. M. Janke, D. J. Dirkes, S. Dovletgeldi, C. Liu, X. Qin, K. Gundogdu, W. You, V. Blum, D. B. Mitzi, *J. Am. Chem. Soc.* **2019**, *141*, 7955.
[31] H. C. Sansom, G. Longo, A. D. Wright, L. R. V. Buizza, M. Zanella, J. T. Gibbon, M. Abda-Jalebi, M. J. Pitcher, M. S. Dyer, T. D. Manning, V. R. Dhanak, R. H. Friend, L. M. Herz, H. J. Snaith, J. B. Claridge, M. J. Rosseinsky, *J. Am. Chem. Soc.* **2021**, *143*, 3983.
[32] C. Liu, Y. Wang, H. Geng, T. Zhu, E. Ertekin, D. Gosztola, S. Yang, J. Huang, B. Yang, K. Han, S. E. Canton, Q. Kong, K. Zheng, X. Zhang, *J. Am. Chem. Soc.* **2019**, *141*, 13074.
[33] A. Q. Wu, X. Xu, R. Venkatasubramanian, *Appl. Phys. Lett.* **2008**, *92*, 011108.
[34] L. Jia, W. Ma, X. Zhang, *Appl. Phys. Lett.* **2014**, *104*, 241911.
[35] M. Scholz, K. Oum, T. Lenzer, *Phys. Chem. Chem. Phys.* **2018**, *20*, 10677.
[36] M. Scholz, O. Flender, K. Oum, T. Lenzer, *J. Phys. Chem. C* **2017**, *121*, 12110.
[37] R. Kentsch, M. Scholz, J. Horn, D. Schlettwein, K. Oum, T. Lenzer, *J. Phys. Chem. C* **2018**, *122*, 25940.
[38] R. P. Feynman, R. W. Hellwarth, C. K. Iddings, P. M. Platzman, *Phys. Rev.* **1962**, *127*, 1004.
[39] M. Schlipf, S. Poncé, F. Giustino, *Phys. Rev. Lett.* **2018**, *121*, 086402.
[40] D. Meggiolaro, F. Ambrosio, E. Mosconi, A. Mahata, F. De Angelis, *Adv. Energy Mater.* **2020**, *10*, 1902748.
[41] H. Fröhlich, *Adv. Phys.* **1954**, *3*, 325.
[42] H. Fröhlich, H. Pelzer, S. Zienau, *London, Edinburgh, Dublin Philos. Mag. J. Sci.* **1950**, *41*, 221.
[43] L. M. Herz, *J. Phys. Chem. Lett.* **2018**, *9*, 6853.
[44] F. Giustino, *Rev. Mod. Phys.* **2017**, *89*, 015003.
[45] W. Bo, N. Weihua, X. Qiang, M. Manukumara, F. Minjun, Y. Senyun, F. Jianhui, L. Stener, Y. Tingting, W. Feng, W. G. Teck, C. H. Padinhare, K. E. T. Yong, X. S. Ze, H. Fuqiang, S. Ranjan, Z. Guofu, G. Feng, S. Tze Chien, *Sci. Adv.* **2021**, *7*, eabd3160.
[46] J. A. Steele, P. Puech, M. Keshavarz, R. Yang, S. Banerjee, E. Debroye, C. W. Kim, H. Yuan, N. H. Heo, J. Vanacken, A. Walsh, J. Hofkens, M. B. Roeffaers, *ACS Nano* **2018**, *12*, 8081.
[47] A. Dey, A. F. Richter, T. Debnath, H. Huang, L. Polavarapu, J. Feldmann, *ACS Nano* **2020**, *14*, 5855.
[48] T. Holstein, *Ann. Phys.* **1959**, *8*, 343.
[49] D. Emin, C. H. Seager, R. K. Quinn, *Phys. Rev. Lett.* **1972**, *28*, 813.
[50] R. Williams, K. Song, *J. Phys. Chem. Solids* **1990**, *51*, 679.
[51] L. R. V. Buizza, A. D. Wright, G. Longo, H. C. Sansom, C. Q. Xia, M. J. Rosseinsky, M. B. Johnston, H. J. Snaith, L. M. Herz, *ACS Energy Lett.* **2021**, *6*, 1729.
[52] E. Papalazarou, J. Faure, J. Mauchain, M. Marsi, A. Taleb-Ibrahimi, I. Reshetnyak, A. V. Roekeghem, I. Timrov, N. Vast, B. Arnaud, L. Perfetti, *Phys. Rev. Lett.* **2012**, *108*, 256808.
[53] M. Hase, K. Mizoguchi, H. Harima, S. ichi Nakashima, K. Sakai, *Phys. Rev. B: Condens. Matter Mater. Phys.* **1998**, *58*, 5448.
[54] Y. Toyozawa, *Prog. Theor. Phys.* **1961**, *26*, 29.
[55] Z. Xiao, W. Meng, J. Wang, D. B. Mitzi, Y. Yan, *Mater. Horiz.* **2017**, *4*, 206.
[56] Z. Xiao, Z. Song, Y. Yan, *Adv. Mater.* **2019**, *31*, 1803792.
[57] M. Scholz, M. Morgenroth, K. Oum, T. Lenzer, *J. Phys. Chem. C* **2018**, *122*, 5854.
[58] S. Koyasu, N. Umezawa, A. Yamaguchi, M. Miyauchi, *J. Appl. Phys.* **2019**, *125*, 115101.
[59] M. Xia, M. Gu, X. Liu, B. Liu, S. Huang, C. Ni, *J. Mater. Sci.: Mater. Electron. 2015 26:7* **2015**, *26*, 5092.
[60] R. N. Bulakhe, N. M. Shinde, R. D. Thorat, S. S. Nikam, C. D. Lokhande, *Curr. Appl. Phys.* **2013**, *13*, 1661.
[61] N. P. Klochko, K. S. Klepikova, V. R. Kopach, I. I. Tyukhov, D. O. Zhadan, G. S. Khrypunov, S. I. Petrushenko, S. V. Dukarov, V. M. Lyubov, M. V. Kirichenko, A. L. Khrypunova, *Sol. Energy* **2018**, *171*, 704.
[62] H. C. Sansom, L. R. V. Buizza, M. Zanella, J. T. Gibbon, M. J. Pitcher, M. S. Dyer, T. D. Manning, V. R. Dhanak, L. M. Herz, H. J. Snaith, J. B. Claridge, M. J. Rosseinsky, *ASC Inorg. Chem.* **2021**.
[63] Z. Hu, Z. Wang, G. Kapil, T. Ma, S. Iikubo, T. Minemoto, K. Yoshino, T. Toyoda, Q. Shen, S. Hayase, *ChemSusChem* **2018**, *11*, 2930.
[64] L. Wang, Y. Bao, S. Wang, F. Wang, C. Xie, K. T. Butler, X. Fan, *Cryst. Growth Des.* **2021**, *21*, 2850.
[65] X.-G. Zhao, D. Yang, J.-C. Ren, Y. Sun, Z. Xiao, L. Zhang, *Joule* **2018**, *2*, 1662.
[66] R. J. Elliott, *Phys. Rev.* **1957**, *108*.
[67] R. E. Brandt, R. C. Kurchin, R. L. Z. Hoye, J. R. Poindexter, M. W. B. Wilson, S. Sulekar, F. Lenahan, P. X. T. Yen, V. Stevanović, J. C. Nino, M. G. Bawendi, T. Buonassisi, *J. Phys. Chem. Lett.* **2015**, *6*, 4297.
[68] J. R. Patnaik, C. S. Sunandana, *J. Phys. Chem. Solids* **1998**, *59*, 1059.
[69] P. S. Kumar, P. B. Dayal, C. S. Sunandana, *Thin Solid Films* **1999**, *357*, 111.
[70] R. I. Biega, M. R. Filip, L. Leppert, J. B. Neaton, *J. Phys. Chem. Lett.* **2021**, *12*, 2057.
[71] M. Fox, *Optical Properties of Solids*, 2nd ed., Oxford University Press, New York, NY **2010**.
[72] P. Y. Yu, M. Cardona, *Fundamentals of Semiconductors : Physics and Materials Properties*, 4th ed., Springer, Berlin, Heidelberg New York **2010**.
[73] K. S. Song, R. T. Williams, *Self-Trapped Excitons*, Springer, Berlin, Heidelberg **1993**.
[74] C. Wehrenfennig, M. Liu, H. J. Snaith, M. B. Johnston, L. M. Herz, *Energy Environ. Sci.* **2014**, *7*, 2269.
[75] L. Buizza, T. Crothers, Z. Wang, J. Patel, R. Milot, H. Snaith, M. Johnston, L. Herz, *Adv. Funct. Mater.* **2019**, *29*.
[76] Z. Xiao, W. Meng, J. Wang, Y. Yan, *ChemSusChem* **2016**, *9*, 2628.
[77] T. Li, X. Zhao, D. Yang, M. H. Du, L. Zhang, *Phys. Rev. Appl.* **2018**, *10*, 041001.
[78] T. Kirchartz, J. A. Márquez, M. Stolterfoht, T. Unold, *Adv. Energy Mater.* **2020**, *10*, 1904134.
[79] A. K. Jena, A. Kulkarni, T. Miyasaka, *Chem. Rev.* **2019**, *119*, 3036.
[80] P. K. Nayak, S. Mahesh, H. J. Snaith, D. Cahen, *Nat. Rev. Mater.* **2019**, *4*, 269.
[81] T. W. Crothers, R. L. Milot, J. B. Patel, E. S. Parrott, J. Schlipf, P. Müller-Buschbaum, M. B. Johnston, L. M. Herz, *Nano Lett.* **2017**, *17*, 5782.
[82] J. M. Richter, M. Abdi-Jalebi, A. Sadhanala, M. Tabachnyk, J. P. Rivett, L. M. Pazos-Outón, K. C. Gödel, M. Price, F. Deschler, R. H. Friend, *Nat. Commun.* **2016**, *7*, 13941.
[83] C. L. Davies, M. R. Filip, J. B. Patel, T. W. Crothers, C. Verdi, A. D. Wright, R. L. Milot, F. Giustino, M. B. Johnston, L. M. Herz, *Nat. Commun.* **2018**, *9*, 293.
[84] G. Lakhwani, A. Rao, R. H. Friend, *Annu. Rev. Phys. Chem.* **2014**, *65*, 557.

[85] C. Groves, N. C. Greenham, *Phys. Rev. B: Condens. Matter Mater. Phys.* **2008**, *78*, 155205.
[86] D. Emin, T. Holstein, *Phys. Rev. Lett.* **1976**, *36*, 323.
[87] V. V. Kabanov, O. Y. Mashtakov, *Phys. Rev. B* **1993**, *47*, 6060.
[88] C. Q. Xia, J. Peng, S. Poncé, J. B. Patel, A. D. Wright, T. W. Crothers, M. U. Rothmann, J. Borchert, R. L. Milot, H. Kraus, Q. Lin, F. Giustino, L. M. Herz, M. B. Johnston, *J. Phys. Chem. Lett.* **2021**, *12*, 3607.
[89] S. A. Bretschneider, I. Ivanov, H. I. Wang, K. Miyata, X. Zhu, M. Bonn, *Adv. Mater.* **2018**, *30*, 1707312.
[90] A. Burgos-Caminal, J. M. Moreno-Naranjo, A. R. Willauer, A. A. Paraecattil, A. Ajdarzadeh, J. E. Moser, *J. Phys. Chem. C* **2021**, *125*, 98.
[91] M. R. Filip, S. Hillman, A. A. Haghighirad, H. J. Snaith, F. Giustino, *J. Phys. Chem. Lett.* **2016**, *7*, 2579.
[92] K. J. Savill, M. T. Klug, R. L. Milot, H. J. Snaith, L. M. Herz, *J. Phys. Chem. Lett.* **2019**, *10*, 6038.
[93] Y. Yang, D. P. Ostrowski, R. M. France, K. Zhu, J. V. D. Lagemaat, J. M. Luther, M. C. Beard, *Nat. Photonics* **2016**, *10*, 53.
[94] M. B. Price, J. Butkus, T. C. Jellicoe, A. Sadhanala, A. Briane, J. E. Halpert, K. Broch, J. M. Hodgkiss, R. H. Friend, F. Deschler, *Nat. Commun.* **2015**, *6*, 8420.
[95] L. M. Herz, *ACS Energy Lett.* **2017**, *2*, 1539.
[96] A. H. Slavney, B. A. Connor, L. Leppert, H. I. Karunadasa, *Chem. Sci.* **2019**, *10*, 11041.
[97] E. M. Hutter, M. C. Gélvez-Rueda, A. Osherov, V. Bulović, F. C. Grozema, S. D. Stranks, T. J. Savenije, *Nat. Mater.* **2017**, *16*, 115.
[98] V. D'Innocenzo, G. Grancini, M. J. P. Alcocer, A. R. S. Kandada, S. D. Stranks, M. M. Lee, G. Lanzani, H. J. Snaith, A. Petrozza, *Nat. Commun.* **2014**, *5*, 3586.
[99] A. C. Dakshinamurthy, C. Sudakar, *Appl. Phys. Lett.* **2021**, *118*, 131902.
[100] A. H. Slavney, L. Leppert, D. Bartesaghi, A. Gold-Parker, M. F. Toney, T. J. Savenije, J. B. Neaton, H. I. Karunadasa, *J. Am. Chem. Soc.* **2017**, *139*, 5015.
[101] E. M. Hutter, M. C. Gélvez-Rueda, D. Bartesaghi, F. C. Grozema, T. J. Savenije, *ACS Omega* **2018**, *3*, 11655.
[102] K.-Z. Du, W. Meng, X. Wang, Y. Yan, D. B. Mitzi, *Angew. Chem., Int. Ed.* **2017**, *56*, 8158.
[103] L. Schade, S. Mahesh, G. Volonakis, M. Zacharias, B. Wenger, F. Schmidt, S. V. Kesava, D. Prabhakaran, M. Abdi-Jalebi, M. Lenz, F. Giustino, G. Longo, P. G. Radaelli, H. J. Snaith, *ACS Energy Lett.* **2021**, *6*, 1073.
[104] S. Li, J. Luo, J. Liu, J. Tang, *J. Phys. Chem. Lett.* **2019**, *10*, 1999.